Journal of Materials Chemistry A

Accepted Manuscript

ROYAL SOCIETY OF CHEMISTRY

www.rsc.org/materialsA

Journal Name

ARTICLE

Nitrogen- and Oxygen-Enriched 3D Hierarchical Porous Carbon fiber: Synthesis and Superior Supercapacity

Received 00th January 20xx,
Accepted 00th January 20xx

DOI: 10.1039/x0xx00000x
www.rsc.org/

Ying Li[a,b], Chunxiang Lu[a], Shouchun Zhang[*a], Fang Yuan Su[c], Wenzhong Shen[d], Pucha Zhou[a], Canliang Ma[e]

Nitrogen- and oxygen-enriched hierarchical porous carbon fiber was fabricated by the phase-separable wet-spinning and the subsequent chemical activation of polyacrylonitrile (PAN) precursor. The wet-spinning could readily offer an interpenetrating 3D meso-/macro-porous network owing to the phase-separation of PAN in the coagulation bath (DMSO/H_2O), caused by the different solubility of PAN in DMSO and H_2O, and the different content of PAN in fiber and the coagulation bath. The later chemical activation introduced abundant small-sized nanopores within the meso-/macro-porous network skeleton. The obtained hierarchical porous carbon fiber exhibited high specific surface area of 2176.6 $m^2 g^{-1}$, large pore volume of 1.272 $cm^3 g^{-1}$, and was highly doped by heteroatoms of nitrogen and oxygen. When it was used as supercapacitor electrodes, high performance of reversible specific capacitances of 329 F g^{-1} at 0.1 A g^{-1} and 223 F g^{-1} at 20 A g^{-1} as well as the capacitance retention of 97.6% after 2000 cycles were achieved in a two-electrode cell.

1. Introduction

Supercapacitors, also known as electrochemical capacitors, have drawn extensive attention due to their shorter charging time, longer cycle life and higher power density. Supercapacitors could fill the energy gap between conventional dielectric capacitors and rechargeable batteries because of their higher energy density than conventional dielectric capacitors and better power density than rechargeable batteries. As a result, supercapacitors are widely used as backup/auxiliary power sources for hybrid electric vehicles, portable electronic devices and large industrial equipments.[1-4]

Carbonaceous materials are the main candidates for supercapacitor electrode materials due to their lower cost, more stable physicochemical properties and better conductivity.[1, 5] Various carbonaceous materials, such as graphenes[6], carbon nanotubes[7], carbon aerogels[8], activated carbons[9, 10], ordered mesoporous carbons[11], nanofibers[12, 13] and hierarchical porous carbons[14-17], have been investigated for supercapacitor electrode materials. Among all carbonaceous materials, activated carbons are widely used as electrode materials due to their high specific area[1, 18]. However, the random porous connectivity and narrow channels in activated carbons slow down the ion transfer from electrolytic solution to the inner surface, especially at high current loads, thus are detrimental to the rate performance. The ordered mesoporous carbons overcome the above difficulty for the low resistance of ions transfer, but possess lower specific area and finite capacitance. Recently, 3D Hierarchical porous carbons show an amazing electrochemical performance because of their unique microstructure: macropores as the ion-buffering reservoirs decrease the diffusion distance of ions to inner surface; mesopores provide low-resistance pathways for ion transfer; micropores are optimal in electric double-layer formation[4, 15-17].

Nowadays, the researchers have developed various methods to obtain 3D hierarchical porous carbon, such as dual-template method[19], pyrolysis of self-assembled block copolymer[20], and the combination of activation and template, activation and electrospinning, template and electrospinning method[15, 21-23]. Although much progress has been made in these methods, their tedious synthesis processes and high cost impose restrictions on wide application and large-scale production. What is more, it remains a great challenge to construct an interpenetrating 3D hierarchical porous network.

Herein, a hierarchical porous carbon fiber (HPCF) with an interpenetrating 3D meso-/macroporous network and abundant small-sized nanopores within the skeleton of the network was fabricated by scalable phase-separable wet-spinning and subsequent chemical activation of polyacrylonitrile (PAN) precursor. The interpenetrating 3D

[a] *National Engineering Laboratory for Carbon Fiber Technology, Institute of Coal Chemistry, Chinese Academy of Sciences, Taiyuan 030001, China. E-mail: zschun@sxicc.ac.cn*
[b] *University of Chinese Academy of Sciences, Beijing 100049, China.*
[c] *Key Laboratory of Carbon Materials, Institute of Coal Chemistry, Chinese Academy of Sciences, Taiyuan 030001, China.*
[d] *State Key Laboratory of Coal Conversion, Institute of Coal Chemistry, Chinese Academy of Sciences, Taiyuan 030001, China.*
[e] *Key Laboratory of Materials for Energy Conversion and Storage of Shanxi Province , Institute of Molecular Science, Shanxi University, Taiyuan 030006, China.*
†Electronic Supplementary Information (ESI) available: SEM and TEM images, the porous structure parameters, XRD patterns, electrochemical capacitive performances using a two-electrode and a three-electrode cell.. See DOI: 10.1039/x0xx00000x

meso-/macro-porous network could readily form into fiber during wet-spinning owing to the phase-separation of PAN in the coagulation bath (DMSO/ H_2O). The phase-separation was caused by the solubility differences of PAN between DMSO and H_2O, and the concentration differences between the fiber and the coagulation bath. The 3D meso-/macro-porous network was still kept after pre-oxidation and carbonization. Usually, the activation of carbon fiber with micrometer scale was so difficult that only nanopores were generated on the surface with random connectivity and narrow channels. In this work, the meso-/macropores within the fiber exhibited good connectivity and promoted the activation efficiency. Therefore, numerous small-sized nanopores formed within the skeleton of the network after activation. In addition, the large-scale production of the precursor fiber could be carried out by wet-spinning method.

Moreover, PAN was selected as precursors to fabricate hierarchical porous carbon fiber, efficiently resulting in high content of nitrogen and oxygen. The nitrogen and oxygen functionalities were proved electrochemically active due to pseudocapacitance and they could significantly improved surface wettability[7, 24-28]. In the present work, the 3D hierarchical porous carbon fiber with numerous nitrogen and oxygen functionalities was obtained, and the contributions of the microstructure and the heteroatom functionalities to the supercapacitor performances were discussed.

2. Experimental

2.1 Materials

Potassium hydroxide (KOH), polytetrafluoroethylene emulsion (PTFE, 60 wt.%) and acetylene black were purchased from Sinopharm Chemical Reagent Co.. The PAN copolymer was polymerized with acrylonitrile (AN) and itaconic acid according reference [29]. The control sample of the nonporous commercial polyacrylonitrile fiber (NPF) was provided by National Engineering Laboratory for Carbon Fiber Technology, ICC, CAS.

2.2 Preparation of 3D hierarchical porous carbon fiber (HPCF)

PAN fiber with the interpenetrating 3D meso-/macroporous network was fabricated by wet-spinning under the coagulation bath (DMSO/H_2O) concentration of 62 wt.% at 60 °C. The polymer concentration was 20 wt.% in the spinning solution. The obtained fiber was washed with deionized water to remove the residual DMSO, and named as PF. The 3D meso-/macroporous network formed because of phase-separation during coagulation. PF was pre-oxidized in the fluid air under temperature gradients of 190, 220 and 250 °C for 2 h, respectively; then carbonized at 700 °C for 1 h, and named CF. The as-derived CF was activated with KOH/CF weight ratio of 2:1 at 700 °C for 1 h. The carbonization and the subsequent activation were carried out in a horizontal tube furnace with a heat rate of 10 °C min^{-1} under N_2 flow rate of 60 ml min^{-1}. The activation products were washed repeatedly with 1 M hydrochloric acid and deionized water till the filtrate became neutral pH, and dried at 100 °C for 12 h, and the hierarchical porous carbon fiber (HPCF) was obtained. The scheme 1 shows the production processes of HPCF. For comparison, the nonporous PAN fiber (NPF) underwent the same sequent thermal treatments as PF, including pre-oxidition, carbonization and activation under the same conditions, and the final sample was named ACF. The names of the products of PF and NPF after each thermal treatment step were listed in Table 1.

Table 1 The product names of PF and NPF after each thermal treatment step.

Sample	Carbonization	Activation
PF	CF	HPCF
NPF	NCF	ACF

2.3 Characterization

The morphology of the samples was characterized by field emission scanning electron microscopy (SEM, JSM-7001F) and transmission electron microscopy (TEM, JEM-2010). The porous texture was analyzed with nitrogen physisorption apparatus (JW-BK122W) at 77K. Before measurement, samples were degassed under vacuum at 200 °C for 6 h. The specific surface area (SSA) and pore size distribution were estimated by Brunauer-Emmett-Teller (BET) and Density Functional Theory (DFT), respectively; the total pore volume (V_{total}) was evaluated from single point adsorption; micropore specific surface area (S_{mic}) was calculated using the t-Plot method; and the mesopore and macropore volume were calculated by the BJH method. Elemental analyses were performed on an elemental analyzer (EA, Vario EL CUBE). The surface chemical properties of the fibers were investigated by X-ray photoelectron spectra (XPS, ESCALAB 250XI) with Al Kα X-ray source (1486.6 eV). The crystallographic structure of the samples was confirmed by X-ray diffraction (XRD, Bruker D8 Advance) with Cu Kα radiation (λ= 0.15406 nm).

2.4 Electrochemical Measurements

Electrochemical properties were recorded on CHI 660E instrument (Shanghai Chenhua Apparatus CO. Ltd.) using a two-electrode cell in 6 M KOH at room temperature. In order to prepare electrodes, the samples were finely powdered in an agate mortar, then mixed with acetylene black and polytetrafluoroethylene (PTFE) binder (weight ratio of 85:10:5) as well as a small amount of ethanol to form slurry. The slurry was coated on the nickel foam (NiF). The prepared electrodes dried at 60 °C overnight. 5-10 mg of the active material was coated on NiF. In the two-electrode cell, the two electrodes with the same size and sample weight were sandwiched together, separated by a polypropylene membrane. Cyclic voltammetry (CV) and galvanostatic charge-discharge (GCD) measurements were implemented in a voltage range of -0.9 to 0 V. Electrochemical impedance spectroscopy (EIS) was performed in the frequency range of 0.01 Hz to 100 kHz with an amplitude of 5 mV at the open circuit potential. The gravimetric capacitance (C, F g^{-1}) was calculated according to the GCD test by the following equation for the two-electrode cells:

$$C = 4\, I\, \Delta t / m\, \Delta V \qquad (1)$$

where *I* (A) is the discharge current, Δt (s) is the discharge time, *m* (g) is the total mass of both carbon electrodes and ΔV (V) is the potential difference.

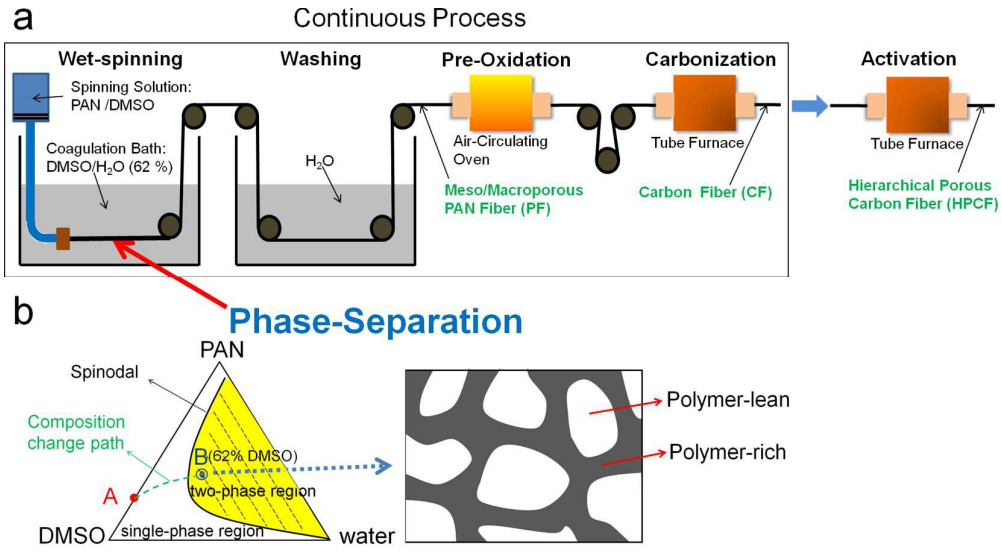

Scheme 1 (a) The schematic diagram of the setup for the preparation of HPCF. The 3D meso-/macroporous network formed because of phase-separation during coagulation. In order to produce more small-sized nanopores, activation was performed. The processes from wet-spinning to carbonization were continuous. (b) The phase diagram of PAN/DMSO/water ternary system (left), and the schematic diagram of the separation phase in point B (right). When the PAN/DMSO jet entered the coagulation bath from the spinneret, the PAN/DMSO/water ternary system formed, and meso-/macroporous network was obtained in the fiber.

3 Results and discussion

3.1 The microstructure of porous carbon fiber samples

The 3D hierarchical porous carbon fiber was fabricated as the steps of the Scheme 1a, among which two steps are critical: phase-separable wet-spinning and activation. Fig. 1 showed the morphology and microstructure of samples after each step. An interpenetrating 3D meso-/macroporous network was observed in the PF (Fig. 1a) because of the phase-separation during the coagulation, which was an essential step of the wet-spinning and significantly affected the microstructure of fiber[29-31]. When the PAN/DMSO jet left the spinneret to enter into the coagulation bath (DMSO/water), the DMSO (solvent) diffused out of the fiber, while the water (nonsolvent) diffused into it due to the concentration difference between the fiber and the coagulation bath. The composition of the single-phase PAN/DMSO solution thereby changed gradually until the spinodal curve was crossed, and then the system entered the unstable two-phase region (as shown in Scheme 1b (left), composition variation path from A to B). As a result, the thermodynamically unstable system separated into polymer-rich and polymer-lean phases, and the polymer-rich phase formed a solid fiber matrix while the polymer-lean phase left a porous structure, as shown in Scheme 1b (right).

The interpenetrating 3D meso-/macroporous network was still kept after carbonization, as shown in Fig. 1(b, c). This was largely due to the pre-oxidation, which stabilized the meso-/macroporous network structure. During pre-oxidation, the cyclization and dehydrogenation reactions led to the formation of the ladder-like molecular structure[32, 33], which enhanced the thermostability and prevented the 3D meso-/macroporous network from collapsing during the high-temperature carbonization.[34, 35] The ladder-like molecules underwent further dehydrogenation and were linked up to form hexatomic ring carbon during carbonization. Thus, the 3D meso-/macroporous network remained, while the shrinkage was inevitable due to the cyclization, dehydrogenation and cross-linked reactions.[32, 34] According to the electron microscope images, the fiber diameter was shrunk from 40 to 28 um, and the pore size reduced from the range of 130-260 nm to 35-140 nm.

In order to increase the microporosity of carbonized fiber, KOH activation was performed. Thus HPCF with numerous small-sized nanopores was obtained. The overall morphology of HPCF was shown in Fig. 2, and the fiber was about 5 cm long. After activation, the 3D meso-/macroporous network had a little enlargement (Fig. 1 (d, e)). From the images, HPCF exhibited a dominant pore size of 45-160 nm and wall thickness of 20-70 nm (that of carbonized fiber was about 30-110 nm). Comparing to the sample before activation, the meso-/macropores were enlarged and the wall thickness became thinner. During activation, further dehydrogenation and cross-linking reactions at high temperature resulted in the shrinkage of framework; the reactions between the surface

atoms and KOH caused the expansion of the meso-/macropore. Both the shrinkage of framework and the expansion of pores contributed to the thinner wall. In addition, many small-sized mesopores within the skeleton of meso-/macroporous network were observed in Fig. 1f. The activation reactions of the surface amorphous carbon generated micropores in the network skeleton. The micopores was developed into mesopores with the activation time.

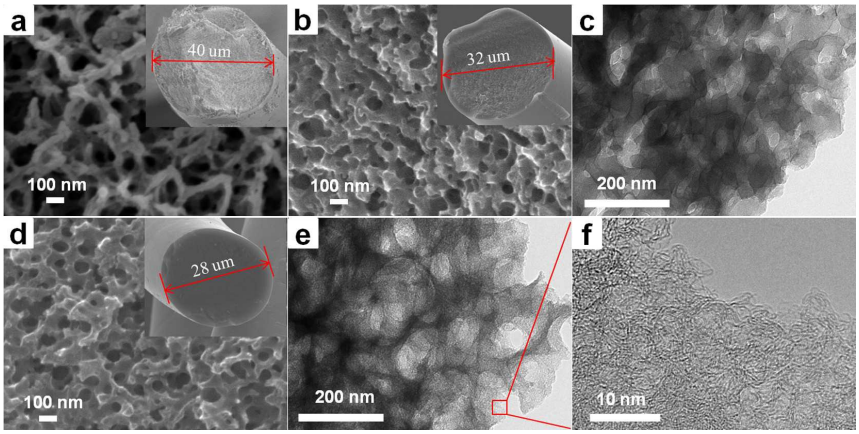

Fig. 1 SEM and TEM images of the cross section of the fiber samples: (a) SEM image of PF, the meso-/macroporous network PAN fiber taken after water washing; (b) SEM and (c) TEM images of CF, the meso-/macroporous carbon fiber derived from PF after carbonization; (d) SEM and (e, f) TEM images of HPCF, the 3D hierarchical porous carbon fiber obtained after activation. The insets in (a, b, d) are the low-resolution SEM images of PF, CF, and HPCF, respectively.

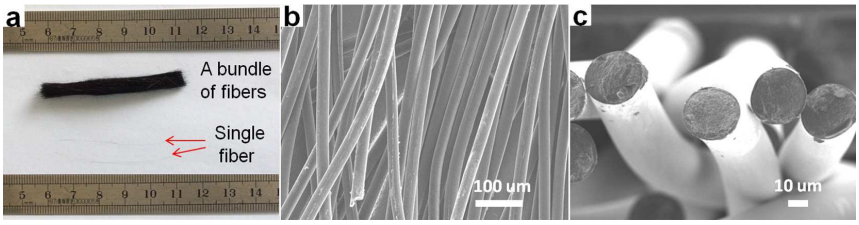

Fig. 2 The overall morphology of HPCF: (a) photograph of a bundle of fibers and single fiber, SEM images of (b) side view and (c) cross section view.

For comparison, the nonporous PAN fiber (NPF) underwent the same heat treatment. As shown in Fig. S1, no visible pores were observed on the SEM and TEM images of NPF and its carbonized and activated samples.

The porous texture of samples was investigated by Nitrogen adsorption isotherms at 77 K. Fig. 3a shows classical type IV adsorption isotherms of PF and its carbonized samples according to the IUPAC classification. PF exhibited a typical capillary condensation step in the pressure (P/P_0) range of 0.8 to 1.0, suggesting the presence of some large mesopores and macropores. After carbonization, it showed the capillary condensation step in the pressure (P/P_0) range of 0.2 to 1.0, and the N_2 adsorption increased slightly at low pressure, implying the shrinkage of meso-/macropores and the formation of a small amount of micropores. The micropores were formed due to the pyrolysis and the subsequent release of small molecules during carbonization[35]. In addition, the sorption hysteresis loops of PF and CF showed the hybrid H1-H3 types because of the good connectivity of the porous network[36]. However, NPF as well as its carbonized derivant showed a type II adsorption isotherm due to the non-porous characteristics. After activation, a combination of type I and IV isotherm (Fig. 3b) was obtained for HPCF, and demonstrated the characteristic curve of a hierarchical porous material. The rapid increase of adsorption at low P/P_0 (close to zero) indicated the presence of micropores; the slow growth of adsorption at P/P_0 below 0.3 suggested the existence of numerous small-sized mesopores. The adsorption hysteresis loop at high P/P_0 (0.9-1.0) showed the hybrid H1-H3 type, which was the same as PF due to excellent connectivity of meso-/macroporous network. As the control sample, ACF exhibited a type I isotherm demonstrating that it was a microporous material. Fig. 3c shows the pore size distribution of the activated fibers. A bimodal distribution appeared for HPCF with one narrow peak at 0.6-1.0 nm and another broad peak at 1.0-3.5 nm, while only one peak at less than 2 nm existed for ACF. The specific surface area and pore volume were listed in Table S1. The total SSA of 2176.6 $m^2 g^{-1}$ and the

total pore volume of 1.272 cm^3 g^{-1} were achieved for HPCF, while less than half corresponding parameters were obtained for ACF. During activation, the 3D porous network facilitated KOH access into the inner side of the fiber and provided more contact area for activation. The more efficient activation resulted in numerous micropores and some developed into mesopores with activation time. The high level activation for HPCF was also confirmed by XRD spectra as shown in Fig. S2. The obviously broad (002) diffraction peak and weaker intensity for HPCF illustrated the disorder microstructure and the destructive crystallite owing to the high level KOH activation[12].

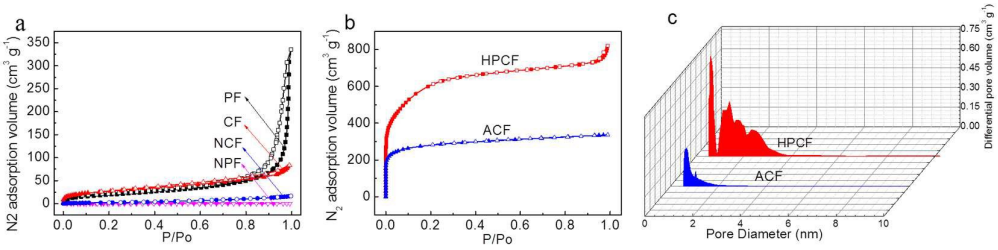

Fig. 3 (a, b) N_2 adsorption/desorption isotherms for PF, NPF and the carbonized and activated samples. NPF was the nonporous PAN fiber as the control sample; NCF and ACF were its carbonized and activated samples, respectively. The solid and hollow symbols represent the adsorption and desorption curves, respectively. (c) The pore size distribution of HPCF and ACF obtained from the DFT method.

3.2 Composition analysis

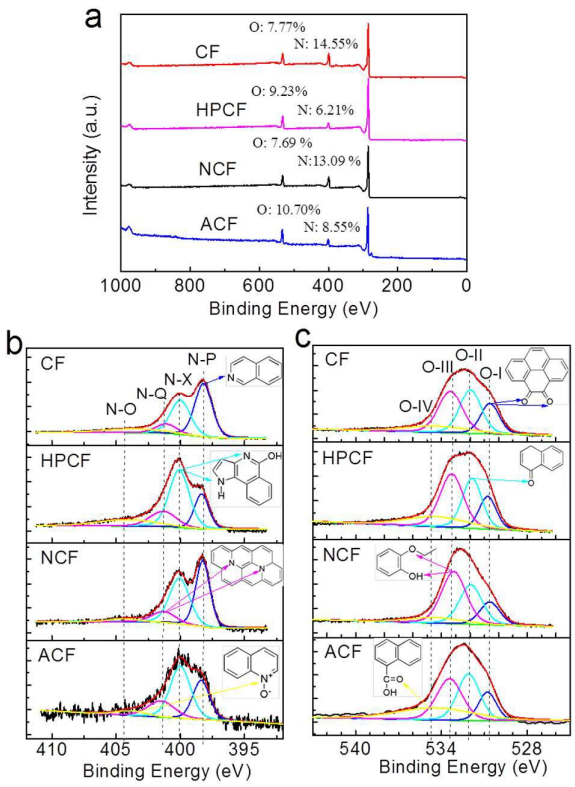

Fig. 4 XPS spectra of samples: (a) the XPS wide-scan spectra, the high resolution for (b) N1s spectra and (c) O1s spectra of samples. CF is the meso-/macroporous carbon fiber derived from PF; HPCF is the hierarchical porous carbon fiber activated from CF; NCF is the nonporous carbon fiber derived from the control fiber (NPF); ACF was activation products of NCF.

It was reported that the heteroatom functionalities affected the electrochemistry properties[26, 37, 38]. Elemental analysis and XPS spectra were performed to evaluate the elemental compositions, and the results was compiled in the Table 2 and Fig. 4. Both elemental analysis and XPS spectra confirmed the presences of nitrogen and oxygen in each sample. The nitrogen was inherited from PAN precursor, and the oxygen not only originated from the comonomer (itaconic acid) of precursor but also was introduced by pre-oxidation and activation[23, 39]. The elemental analysis exhibited the same trend with the XPS spectra. The N or O content of CF and NCF was similar due to the same precursor and heat treatment. After activation, the N content for HPCF and ACF was significantly decreased, while the O content had a slight increase after activation. The similar results were reported in other literatures[12, 18]. XPS is useful for surface chemistry characterization, thus high resolutions for N 1s and O1s were performed to analyze surface elemental state as shown in Fig. 4(b, c). The N 1s high resolution spectra were deconvoluted into four peaks: pyridinic nitrogen (N-P, 398.5 ± 0.3 eV), mixture of pyridone and pyrrolic nitrogen (N-X, 400.3 ± 0.3 eV), quaternary nitrogen (N-Q, 401.2 ± 0.3 eV) and pyridine oxide nitrogen (N-O, 403-405 eV).[20, 40, 41] The O 1s spectra were fitted to four peaks including C=O quinine type group (O-I, 530.7± 0.2 eV), carbon-oxygen double bond (O-II, 531.9± 0.2 eV), carbon-oxygen ether-like single bond and/or carbon-oxygen single-bond in hydroxyl groups (O-III, 533.3 ± 0.2 eV) and chemisorbed oxygen (carboxylic groups) and/or water (O-IV, 534.2± 0.2 eV) [7, 12, 20, 25]. The content of N-P and N-X for HPCF and ACF significantly decreased because of the consumption of the surface atoms during the chemical activation reactions, while the content variation of N-Q (entrapped within a carbon lattice) was not obvious. It was proved that N-P, N-X and O-I were electrochemically active and provided pseudocapacitance; N-Q improved the electric conductivity

and decreased the internal resistance for supercapacitors.[12, 26, 42] In addition, the nitrogen- and oxygen-containing functionalities improved the wettability in the aqueous electrolyte and decreased the contact resistance of the interface between carbon material and electrolyte.[7, 26] The influence of the nitrogen and oxygen atoms of the samples on the performances of supercapaitors will be discussed in the following parts.

Table 2 The content of elemental compositions and surface functional groups for CF, NCF, HPCF and ACF.

Sample	EA[a] (wt.%)				XPS (at.%)			Content of N functional groups[b] (at.%)				Content of O functional groups[b] (at.%)			
	C	N	O	H	C	N	O	N-P	N-X	N-Q	N-O	O-I	O-II	O-III	O-IV
CF	73.60	16.12	7.62	2.06	77.68	14.55	7.77	6.69	4.87	1.43	1.56	1.50	2.51	2.67	1.10
NCF	74.75	16.98	7.56	1.79	79.22	13.09	7.69	5.56	5.48	1.54	0.48	1.20	2.35	2.35	0.78
HPCF	81.07	7.54	8.21	1.14	84.56	6.21	9.23	1.28	2.94	1.04	0.95	1.50	2.62	2.62	1.72
ACF	75.95	10.27	12.81	1.91	80.75	8.55	10.70	2.52	3.95	1.63	0.53	1.53	3.13	3.13	2.93

[a] Derived from CHNO elemental analysis. [b] Derived from XPS, (N-P + N-X + N-Q + N-O) (at.%) = N (at.%) and (O-I + O-II + O-III + O-IV) (at.%) = O (at.%)

3.3 Electrochemical performance

In order to investigate the electrochemical performance of the above four nitrogen- and oxygen-enriched carbonized and activated samples, CV, GCD and EIS were performed in a two-electrode cell. The CV curves of the four samples at different scan rates are shown in Fig. 5(a, b) and S3. HPCF exhibited a slightly distorted rectangular CV curve with the largest area and a well-broadened wide reversible hump (as shown in Fig. 5a), suggesting good capacitive performance. It was attributed to the large SSA and abundant nitrogen- and oxygen-containing functionalities providing more active sites for electric double-layer formation and Faradic redox reactions. CV curve of ACF was similar to that of HPCF, but possessed a smaller area due to the lower SSA. As for NCF, the CV curve exhibited the smallest area and an unapparent hump despite high content of nitrogen and oxygen, mainly attributed to the bare pore structure (S_{BET} = 8.5 m^2 g^{-1}). The results could be explained by that the charge separation and Faradic redox reactions were interface-bound reactions[24]. Therefore, high content of electrochemically active heteroatoms alone could not achieve good capacitive performances without high SSA. For the same reason, CF also showed small area and vague hump for CV curve. When the scan rate increased from 2 to 300 mV s^{-1}, the CV curve still remained rectangular shape for HPCF as well as CF, while was obviously distorted for ACF and NCF (as shown in Fig. 5b and S3), implying faster ion transfer for HPCF and CF at high scan rate. It was mainly due to the promotion effect of the 3D interpenetrating meso-/macroporous network and appropriate small-sized mesopores on the ion transfer and response. However, the nonporous structure for NCF and the narrow micropore size distribution for ACF are unfavourable for quick ion diffusion.

The GCD curves of samples at the current density of 0.1 A g^{-1} are shown in Fig. 5c. The specific capacitances were evaluated on the basis of the GCD according to the equation (1), and the capacitances of 95 F g^{-1} for NCF, 161 F g^{-1} for CF, 244 F g^{-1} for ACF, and 329 F g^{-1} for HPCF were obtained. The highest specific capacitance for HPCF was contributed by both double-layer capacitance and pseudocapacitance. In general, a straight line of charge-discharge curve was characteristic of the electric double-layer supercapacitor. The deviation to linearity for all GCD curve confirmed the existence of the Faradic capacitance, which were provided by electrochemically active nitrogen and oxygen functionalities. As shown in Fig. 4 and Table 2, the electrochemically active nitrogen and oxygen (N-P, N-X, and O-I) still remained considerable content after activation. Fig. 5d showed the GCD curves of all sample at the current density of 10 A g^{-1}. All samples except NCF still kept nearly linear and symmetrical GCD curves with gradual slope changes at high current density, implying good capacitive performance and electrochemical reversibility. The GCD curve of NCF could not reach the top for little charges were accumulated with bare pore structure. ACF exhibited obvious ohmic drops, while a smaller one was observed for CF and the smallest one for HPCF, indicating the lowest overall resistance for the HPCF cell. The results agreed with the Nyquist plots presented in Fig. 5e. The small semicircle at the high frequency and the short 45° diagonal at the intermediate frequency were observed for HPCF, because the low resistance for charge and ion transfer due to the 3D hierarchical porous structure. The almost vertical line at low frequency for HPCF suggested an excellent capacitive behaviour without diffusion limitations. In addition, every sample exhibited a small initial non-zero intercept at the real impedance axis, partly due to the good wettability endowed by the nitrogen- and oxygen-containing functionalities.

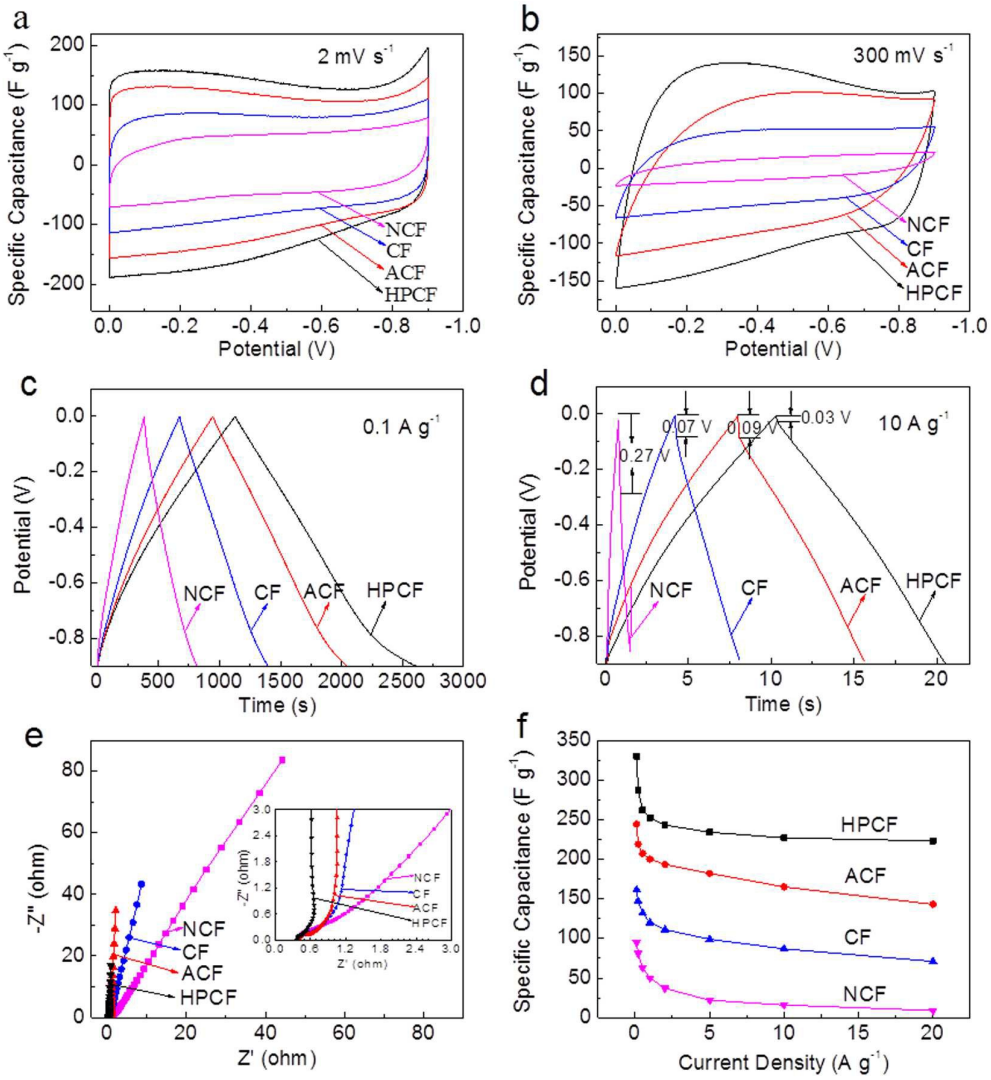

Fig. 5 CV curves at the scan rate of (a) 2 mV s^{-1} and (b) 300 mV s^{-1}, GCD curves at the current density of (c) 0.1 A g^{-1} and (d) 20 A g^{-1}, (e) Nyquist plots at amplitude of 5 mV and (f) specific capacitances as a function of current densities at the range of 0.1-20 A g^{-1} for NCF, CF, ACF, and HPCF.

The rate performance is important for supercapacitor in practical application. The specific capacitances at different current densities from 0.1 to 20 A g^{-1} were evaluated by GCD curves, as shown in Fig. 5f and S4. The specific capacitance of each sample decreased with the current density increase. The specific capacitances remained 9 F g^{-1} for NCF, 71 F g^{-1} for CF, 147 F g^{-1} for ACF and 223 F g^{-1} for HPCF, with retention of 9.5%, 44.1%, 60.2% and 67.8%, respectively. HPCF presented the excellent rate performance owing to the 3D hierarchical porous structure. The rate property was also demonstrated by the CV curves at scan rate range of 2-300 mV s^{-1} (Fig. S3a). The CV curves showed small changes in shape and area with the scan rate increasing.

The CV, GCD and EIS characterizations were quite consistent with each other. The high specific capacitance for HPCF was provided by both the developed 3D hierarchical pores and the high content of nitrogen and oxygen functionalities. Pores between 0.6-1.0 nm were most effective in double-layer formation due to the good correlation with the size of hydrated ions[25]. The macropores and large mesopores acted as ion-buffering reservoirs for electrolyte ions, and shortened the diffusion distance of ions to the inner surface. The small-sized mesopores within the skeleton provided low-resistant pathways for ions, facilitating ions fast adsorption and release during charging and discharging. Therefore, HPCF exhibited low overall resistance and remained much capacitance at large current loads, resulting excellent rate performance. As for ACF, the dominant micropores with poor meso-/macropores exhibited large diffusion resistance and inefficient use at large current loads, leading to the partial capacitance loss. CF with developed meso-/macroporous network showed low overall resistance but low capacitance

owing to the less interface-bound reactions in few micropores. NCF with bare pore structure exhibited the least capacitance and the poorest rate performance because of little interface-bound reactions and large overall resistance. Therefore, the developed 3D hierarchical pores played a key role in the superior supercapacitive performances.

Table 3 The comparison of the capacitances of some typical carbon materials in the literatures.

Precursor	S_{BET} (m^2 g^{-1})	S_{micro} (m^2 g^{-1})	V_{total} (m^3 g^{-1})	V_{meso} (m^3 g^{-1})	N (at.%)	O (at.%)	Electrolyte	C_{high} (F g^{-1})	Cell	Ref.
Furfuryl alcohol	709	-	0.88	0.61	-	-	KOH	221 (1 A g^{-1})	3E	43
CH_4	140	-	0.337	0.289	-	14.5	KOH	20 (0.2 A g^{-1})	3E	44
							H_2SO_4	15 (0.2 A g^{-1})		
Phenolic	545	500	0.26	0.03	-	10	KOH	256 (0.2 A g^{-1})	2E	23
POF	525	-	0.67	-	4.73	-	KOH	230 (0.5 A g^{-1})	3E	45
Chitin	1000	69	0.88	-	4.6	-	H_2SO_4	183 (0.23 A g^{-1})	2E	37
Melanine	8	-	-	-	13.3	1.4	KOH	198 (0.1 A g^{-1})	2E	46
							H_2SO_4	115 (0.1 A g^{-1})		
EDTA	708	-	-	-	7.7	8.2	KOH	245 (0.05 A g^{-1})	2E	42
Carneum gigeriae gali	2149.9	-	0.95	0.68	2.04	4.32	KOH	198 (1 A g^{-1})	3E	47
Gelatin	1518	42	4.27	4.14	2.12	10.84	KOH	284.1 (1 A g^{-1})	3E	19
Polypyrrole	706	-	-	-	19.8	11.1	H_2SO_4	384.9 (0.5 A g^{-1})	3E	7
PAN	508	222	1.03	0.93	18.63	7.75	H_2SO_4	155 (0.1 A g^{-1})	2E	48
	635	268	1.56	1.47	15.61	6.3		210 (0.1 A g^{-1})		
	608	236	1.87	1.79	7.78	8.32		161 (0.1 A g^{-1})		
PAN	1300	970	0.63	0.06	-	-	H_2SO_4	290 (1 mA)	2E	49
PAN	8.5	-	0.026	-	13.09	7.69	KOH	95 (0.1 A g^{-1})	2E	NCF
	98.9	13.3	0.129	0.128	14.55	7.77		161 (0.1 A g^{-1})		CF
	1002.9	827.9	0.521	0.208	8.55	10.7		244 (0.1 A g^{-1})		ACF
	2176.6	1730.7	1.272	0.74	6.21	9.23		329 (0.1 A g^{-1})		HPCF

In order to clearly illustrate the contribution of porous texture and heteroatoms on high capacitance of HPCF, comparisons with other reported nitrogen or/and oxygen enriched carbons are listed in Table 3. The capacitance value in each contrast reference was calculated by the same equation as this paper, and the electrochemical measurement was performed in the KOH/H_2SO_4 aqueous electrolyte. From the comparison, it clearly revealed that the higher SSA and nitrogen or/and oxygen content, the higher specific capacitance was achieved. However, high heteroatoms content without high SSA could not lead to high specific capacitance[44, 46] because of the less interface-bound reactions. In addition, the low microporosity resulted in low capacitance because micropores were most effective in double-layer formation [19, 37, 48]. The same precursor of PAN[48, 49] was used as this work, but HPCF in this work exhibited the best capacitive performance. The high mesoprosity (more than 90%) of NPC[48] limited charges to accumulate and few nitrogen and oxygen atoms was remained after such high temperature heat treatment (carbonization and CO_2 activation at 900 °C)[49]. The activated carbon nanotube[7] derived from polypyrrole exhibited better capacitive performance despite lower SSA than HPCF, and it could be explained by the higher contents of nitrogen and oxygen, especially, the electrochemically active nitrogen (pyridinic and pyridine/pyrrolic nitrogen). Therefore, high SSA, optimal pore size, and enriched heteroatoms contributed to high specific capacitance.

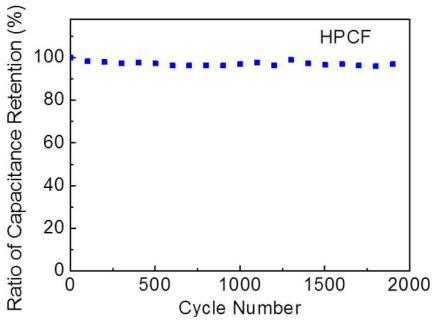

Fig. 6 Cycling stability of HPCF at the current density of 2 A g^{-1}.

The cycle stabilization of HPCF was investigated by GCD cycling at the current density of 2 A g^{-1}. After 2000 cycles, the specific capacitance still retained 97.6%, as shown in Fig 6, demonstrating good cycle stability. This excellent cycle stability

of HPCF was attributed to the stable porous structure and covalent connectivity between functionalities and carbons.

The CV and GCD were also performed in a three-electrode configuration. The samples exhibited the similar CV and GCD curves with the corresponding tests in a two-electrode cell, as shown in Fig. S5. The specific capacitances of 142 F g^{-1} for NCF, 214 F g^{-1} for CF, 256 F g^{-1} for ACF, and 348 F g^{-1} for HPCF at 0.1 A g^{-1} were obtained. When the current density increased to 20 A g^{-1}, the specific capacitance still remained 16 F g^{-1} for NCF, 98 F g^{-1} for CF, 153 F g^{-1} for ACF and 227 F g^{-1} for HPCF. The results obtained from the three-electrode and two-electrode systems were quite consistent with each other.

4. Conclusions

In the present work, we have fabricated the interpenetrating 3D hierarchical porous carbon fiber doped with numerous nitrogen and oxygen atoms. It was fascinating that the meso-/macroporous network readily formed in the fiber during phase-separable wet-spinning. After activation, many small-sized nanopores were produced within the skeleton of the meso-/macroporous network, resulting in good connectivity of the hierarchical pore. The obtained HPCF exhibited the high SSA (2176.6 m^2 g^{-1}) and pore volume (1.272 cm^3 g^{-1}), and high content of nitrogen and oxygen. The unique structures and abundant nitrogen and oxygen endowed HPCF with not only excellent specific capacitance of 329 F g^{-1} at 0.1 A g^{-1}, but also promising rate performance with capacitance retention of 67.8% at 20 A g^{-1}. In addition, HPCF demonstrated the good cycle stability with capacitance retention of 97.6% after 2000 cycles. The results suggest that HPCF is a very attractive material for potential application in electrochemical energy storage.

Acknowledgements

The authors are grateful to Professor Junzhong Wang for the practical guidance and the reviewers for their valuable comments. The financial supports from National Natural Science Foundation of China (No. 50602045) and Key Program of the Chinese Academy of Sciences (No. K125-12-002) are gratefully acknowledged.

References

1 P. Simon and Y. Gogotsi, Nat Mater, 2008, 7, 845-854.
2 G. Wang, L. Zhang and J. Zhang, Chemical Society reviews, 2012, 41, 797-828.
3 Y. Zhai, Y. Dou, D. Zhao, P. F. Fulvio, R. T. Mayes and S. Dai, Advanced Materials, 2011, 23, 4828-4850.
4 H. Jiang, P. S. Lee and C. Li, Energy & Environmental Science, 2013, 6, 41-53.
5 P. Sharma and T. S. Bhatti, Energy Conversion and Management, 2010, 51, 2901-2912.
6 J. Hu, Z. Kang, F. Li and X. Huang, Carbon, 2014, 67, 221-229.
7 Z. Zhou, Z. Zhang, H. Peng, Y. Qin, G. Li and K. Chen, RSC Advances, 2014, 4, 5524-5530.
8 D. Liu, J. Shen, N. Liu, H. Yang and A. Du, Electrochimica Acta, 2013, 89, 571-576.
9 D. Bhattacharjya and J.-S. Yu, Journal of Power Sources, 2014, 262, 224-231.
10 X. Xiang, E. Liu, L. Li, Y. Yang, H. Shen, Z. Huang and Y. Tian, J Solid State Electrochem, 2011, 15, 579-585.
11 W. Xing, S. Z. Qiao, R. G. Ding, F. Li, G. Q. Lu, Z. F. Yan and H. M. Cheng, Carbon, 2006, 44, 216-224.
12 C. Ma, Y. Li, J. Shi, Y. Song and L. Liu, Chemical Engineering Journal, 2014, 249, 216-225.
13 F. Zhang, C. Yuan, J. Zhu, J. Wang, X. Zhang and X. W. Lou, Advanced Functional Materials, 2013, 23, 3909-3915.
14 D.-W. Wang, F. Li, M. Liu, G. Q. Lu and H.-M. Cheng, Angewandte Chemie International Edition, 2008, 47, 373-376.
15 Y. S. Yun, C. Im, H. H. Park, I. Hwang, Y. Tak and H.-J. Jin, Journal of Power Sources, 2013, 234, 285-291.
16 Y. Liang, F. Liang, H. Zhong, Z. Li, R. Fu and D. Wu, Journal of Materials Chemistry A, 2013, 1, 7000-7005.
17 L. Wan, J. Wang, L. Xie, Y. Sun and K. Li, ACS Appl Mater Interfaces, 2014, 6, 15583-15596.
18 W. Qiao, S.-H. Yoon and I. Mochida, Energy & Fuels, 2006, 20, 1680-1684.
19 X. Y. Chen, C. Chen, Z. J. Zhang and D. H. Xie, Journal of Materials Chemistry A, 2013, 1, 10903-10911.
20 M. Zhong, E. K. Kim, J. P. McGann, S. E. Chun, J. F. Whitacre, M. Jaroniec, K. Matyjaszewski and T. Kowalewski, J Am Chem Soc, 2012, 134, 14846-14857.
21 W. Xing, C. C. Huang, S. P. Zhuo, X. Yuan, G. Q. Wang, D. Hulicova-Jurcakova, Z. F. Yan and G. Q. Lu, Carbon, 2009, 47, 1715-1722.
22 Y. Y. Lv, F. Zhang, Y. Q. Dou, Y. P. Zhai, J. X. Wang, H. J. Liu, Y. Y. Xia, B. Tu and D. Y. Zhao, Journal of Materials Chemistry, 2012, 22, 93-99.
23 C. Ma, Y. Song, J. Shi, D. Zhang, X. Zhai, M. Zhong, Q. Guo and L. Liu, Carbon, 2013, 51, 290-300.
24 L. Zhao, L. Z. Fan, M. Q. Zhou, H. Guan, S. Qiao, M. Antonietti and M. M. Titirici, Adv Mater, 2010, 22, 5202-5206.
25 D. Hulicova-Jurcakova, M. Seredych, G. Q. Lu and T. J. Bandosz, Advanced Functional Materials, 2009, 19, 438-447.
26 C. Yuan, X. Liu, M. Jia, Z. Luo and J. Yao, Journal of Materials Chemistry A, 2015, 3, 3409-3415.
27 F. Su, C. K. Poh, J. S. Chen, G. Xu, D. Wang, Q. Li, J. Lin and X. W. Lou, Energy Environ. Sci., 2011, 4, 717-724.
28 H. Luo, Z. Liu, L. Chao, X. Wu, X. Lei, Z. Chang and X. Sun, Journal of Materials Chemistry A, 2015, 3, 3667-3675.
29 J. Hao, C. Lu, P. Zhou and D. Li, Thermochimica Acta, 2013, 569, 42-47.
30 P. Zhou, C. Lu, J. Shi, K. Li, F. He, S. Zhang and Y. Li, Journal of Macromolecular Science, Part B, 2011, 50, 1215-1225.
31 X.-G. Dong, C.-G. Wang, Y.-J. Bai and W.-W. Cao, Journal of Applied Polymer Science, 2007, 105, 1221-1227.
32 I. Karacan and G. Erdogan, Fibers Polym, 2012, 13, 295-302.
33 X.-H. Qin, J Therm Anal Calorim, 2010, 99, 571-575.
34 X. Meng, H. Cui, J. Dong, J. Zheng, Y. Zhu, Z. Wang, J. Zhang, S. Jia, J. Zhao and Z. Zhu, Journal of Materials Chemistry A, 2013, 1, 9469-9476.
35 M. S. A. Rahaman, A. F. Ismail and A. Mustafa, Polymer Degradation and Stability, 2007, 92, 1421-1432.

36 F. Rojas, I. Kornhauser, C. Felipe, J. M. Esparza, S. Cordero, A. Domínguez and J. L. Riccardo, Physical Chemistry Chemical Physics, 2002, 4, 2346-2355.
37 T.-D. Nguyen, K. E. Shopsowitz and M. J. MacLachlan, Journal of Materials Chemistry A, 2014, 2, 5915-5921.
38 K. Fujisawa, R. Cruz-Silva, K.-S. Yang, Y. A. Kim, T. Hayashi, M. Endo, M. Terrones and M. S. Dresselhaus, Journal of Materials Chemistry A, 2014, 2, 9532-9540.
39 C. O. Ania, V. Khomenko, E. Raymundo-Piñero, J. B. Parra and F. Béguin, Advanced Functional Materials, 2007, 17, 1828-1836.
40 R. Arrigo, M. Hävecker, S. Wrabetz, R. Blume, M. Lerch, J. McGregor, E. P. J. Parrott, J. A. Zeitler, L. F. Gladden, A. Knop-Gericke, R. Schlögl and D. S. Su, Journal of the American Chemical Society, 2010, 132, 9616-9630.
41 S. Biniak, G. Szymański, J. Siedlewski and A. Świątkowski, Carbon, 1997, 35, 1799-1810.
42 B. Xu, D. Zheng, M. Jia, G. Cao and Y. Yang, Electrochimica Acta, 2013, 98, 176-182.
43 Q. Zhao, X. Wang, C. Wu, J. Liu, H. Wang, J. Gao, Y. Zhang and H. Shu, Journal of Power Sources, 2014, 254, 10-17.
44 A. Śliwak, B. Grzyb, J. Ćwikła and G. Gryglewicz, Carbon, 2013, 64, 324-333.
45 X. Liu, L. Zhou, Y. Zhao, L. Bian, X. Feng and Q. Pu, ACS Applied Materials & Interfaces, 2013, 5, 10280-10287.
46 D. Hulicova-Jurcakova, M. Kodama, S. Shiraishi, H. Hatori, Z. H. Zhu and G. Q. Lu, Advanced Functional Materials, 2009, 19, 1800-1809.
47 X. Hong, K. S. Hui, Z. Zeng, K. N. Hui, L. Zhang, M. Mo and M. Li, Electrochimica Acta, 2014, 130, 464-469.
48 X. Yang, D. Wu, X. Chen and R. Fu, The Journal of Physical Chemistry C, 2010, 114, 8581-8586.
49 K.-P. Wang and H. Teng, Carbon, 2006, 44, 3218-3225.
50

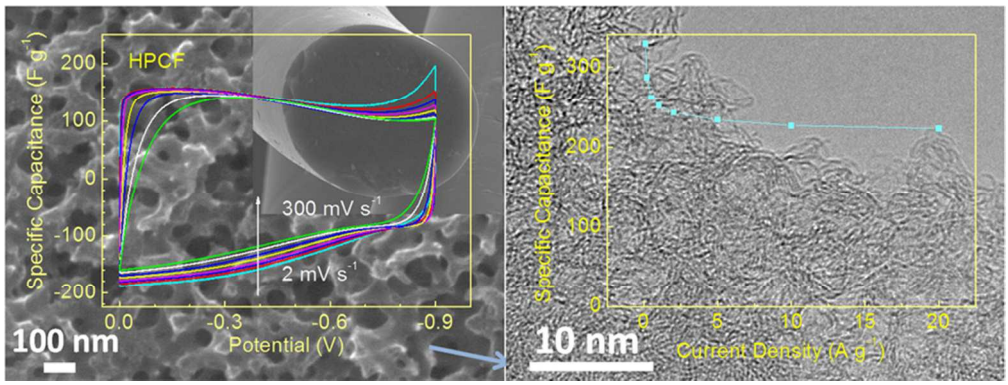

The 3D hierarchical porous carbon fiber was fabricated by the phase-separable wet-spinning and the subsequent activation for high-performance supercapacitor.
80x30mm (300 x 300 DPI)